

Chapter 5

Photodissociation and recombination of solvated I_2^- : What causes the transient absorption peak?

Seven years ago, Lineberger and co-workers observed evidence of coherent nuclear motion in the photodissociation and recombination of I_2^- clustered with CO_2 [1–3]. In their experiment, a 720 nm pulse excites the I_2^- chromophore to its repulsive A' state (Fig. 5.1). Dissociation of the chromophore makes the cluster transparent, allowing recombination to be monitored with a subsequent 720 nm probe pulse. Assuming that the excited clusters dispose of their excess energy by evaporation, the mass spectrum of the ionic photofragments enables one to identify those clusters which have absorbed both pulses. By measuring the intensity of this two-photon product channel as a function of time delay between pump and probe, Lineberger and co-workers determined the overall time scale for dissociation, recombination, and vibrational relaxation of the solvated ion. The most striking result of these experiments was a transient peak in the absorption recovery at about 2 ps after excitation, which was attributed to the coherent passage of recombining chromophores through a region of the potential surface characterized by strong absorption. A similar feature has been seen in the dissociation and recombination of I_2^- in liquid solutions [4, 5].

These experiments have stimulated an intensive program of research into the dynamics of I_2^- photodissociation and recombination. Pump-probe experiments have now been carried out on a variety of clusters [6, 7] as well as liquid solutions [4, 5, 8, 9].

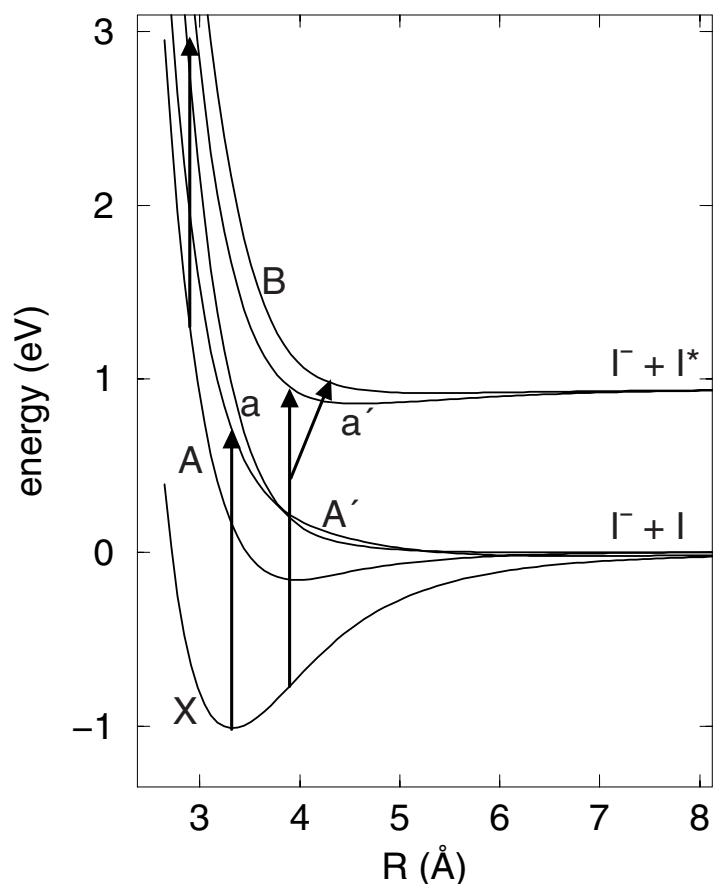


Figure 5.1: Scaled **ab initio** gas phase potential curves for I_2^- . Arrows mark the 720 nm pump absorption ($X \rightarrow A'$), our assignment of the transient absorption peak at 2 ps ($X \rightarrow a', B$) and a previous assignment for the same ($A \rightarrow a$).

Measurements of the absorption recovery in particular mass channels [10] have yielded information about the dynamics of the solvent cage during the recombination process. Femtosecond time-resolved photoelectron spectra (FPES) [11, 12] have provided complementary insights into the mechanisms of recombination and relaxation in these systems. Finally, nonadiabatic molecular dynamics simulations have successfully reproduced the experimental product distributions [13–16], time-resolved photoelectron spectra [17], and the overall absorption recovery [18], and have led to a detailed molecular picture of the dynamics.

A crucial element is missing from the picture, however: the mechanism that gives

rise to the 2 ps transient peak in the absorption recovery has never been conclusively identified. Lineberger and co-workers originally ascribed it to absorption from the inner wall of the weakly bound A state to the higher-lying a state (Fig. 5.1). This assignment is consistent with the polarization dependence of the signal, which shows that the associated transition moment is parallel to the internuclear axis, and with the solution-phase experiments, which found that the transient disappeared when the system was probed with UV radiation [5]. The FPES experiments [12] and the simulations [15, 16, 18] did find significant A -state recombination, but in the simulations the A -state dynamics was observed to be diffusive rather than coherent, and the trajectories did not appear to find regions where the $A \rightarrow a$ transition might be resonant with the probe. Instead, the simulations found that a significant fraction of the ensemble recombined in the **ground** state on this time scale. This suggests that the transient might be due to ground-state absorption, but this could not be demonstrated directly since the simulation statistics were not sufficient to resolve the finer structures in the absorption recovery [18].

In this Chapter we present new simulation results which, we believe, settle this issue. By using a much larger number of trajectories than earlier studies, we are able to resolve the 2 ps transient in the absorption recovery and to show that it is due to transitions from the ground state to the **spin-orbit excited** B and a' states of I_2^- . The absorption occurs at large internuclear distances ($R > 3.7 \text{ \AA}$), as the fragments first recombine, not at the inner turning point. This possibility was considered by Papanikolas et al. [2, 3], but tentatively ruled out because it requires that the spin-orbit energy be efficiently converted into thermal energy of the cluster in order to yield the observed two-photon fragments. The subsequent experimental [7, 19] and theoretical [20] demonstration that spin-orbit quenching is actually extremely efficient in these systems, occurring on a time scale of a few ps, removes this objection. Our new assignment is consistent with the parallel probe transition moment observed in the clusters, and with the absence of a 2 ps transient in the UV probe absorption. Analysis of the simulations

using an electron-transfer perspective described in previous work [15, 16, 20] shows that solvent-induced perturbations of the solute electronic structure play a crucial role in determining the regions of strong absorption. We also report on the simulated absorption recovery of $\text{I}_2^- \text{Ar}_{20}$ which shows a prominent transient feature not observed in the experiments [6]. To investigate this apparent discrepancy we consider the UV photodissociation of $\text{I}_2^- \text{Ar}_n$ clusters. Ultimately, we are forced to reevaluate key assumptions made in interpreting the experiments.

5.1 Methods

The simulations are based on the effective Hamiltonian discussed in Chapter 2. The interaction between the I_2^- solute and the rigid CO_2 solvent molecules is represented by an operator that includes state-dependent electrostatic and induction interactions based on **ab initio** calculations of the solute electronic structure [21] and experimental data for the solvent charge distribution and polarizability. The one-electron density matrix derived from the solute wave functions is expanded in distributed multipole operators [22]. Diagonal elements of these operators describe the solute charge density in various electronic states, while off-diagonal elements describe transition charge densities that allow the solvent to polarize the solute charge density. In the present application these distributed transition moments are also used to assemble the transition dipole matrix elements that determine the optical absorption intensities. State-independent atom-atom Lennard-Jones potentials, fit to reproduce known $\text{I}^- \text{CO}_2$ and $\text{I} \text{CO}_2$ potential curves [23], account for the dispersion and repulsion interactions between solute and solvent, while the $\text{CO}_2 \text{CO}_2$ interaction potential is taken from Murthy et al. [24]. The overall model captures the sensitive dependence of the solute charge distribution on the solute electronic state, the solute bond length, and the positions and orientations of the solvent molecules. At each trajectory time step the Hamiltonian matrix, which depends parametrically upon the coordinates of all the solute and solvent nuclei, is

constructed and diagonalized, yielding the energies, forces, and nonadiabatic transition probabilities required to proceed to the next step. Nuclear motion on a single adiabatic potential surface is computed using the velocity version of the Verlet algorithm [25, 26], while hopping between surfaces is computed using a modified version [16] of Tully's MDQT method [27, 28].

The absorption recovery signal is calculated using the quasiclassical prescription of Coker and coworkers [18, 29]. Along each trajectory, a contribution to the probe absorption is recorded when the energy gap between the occupied state and a higher-lying state falls within a Gaussian window around the probe frequency; these contributions are weighted by the square of the transition dipole moment connecting these states. This signal is given by

$$S(t) \sim \frac{1}{N} \sum_{k=1}^N \sum_f |\mu_{fj_k}[\mathbf{R}_k(t)]|^2 \times \exp\left[-\frac{\{\Delta E_{fj_k}[\mathbf{R}_k(t)] - h\nu_{\text{probe}}\}^2}{2\sigma_E^2}\right]. \quad (5.1)$$

In this expression, N is the number of trajectories, $\mu_{fj_k}[\mathbf{R}_k(t)]$ is the transition dipole matrix element between states i and f at the current nuclear configuration, $\mathbf{R}_k(t)$, and $\Delta E_{fj_k}[\mathbf{R}_k(t)]$ is the energy gap between the initial and final states. This signal is convoluted with a Gaussian pulse in time to model the finite duration of the pump pulse. The final expression for the absorption recovery signal is

$$I(t) \approx \int_{-\infty}^{\infty} dt' \exp\left[-\frac{\{t - t'\}^2}{2\sigma_t^2}\right] S(t'). \quad (5.2)$$

In the results reported here the time width $\sigma_t = 150$ fs, consistent with the experimental value of ≈ 120 fs [2], and the energy width $\sigma_E = 0.005$ a.u.. While this is larger than the value $\sigma_E = 0.001$ a.u., derived from the spectral bandwidth in the femtosecond experiments of Papanikolas et al., we find that varying σ_E from 0.0001 a.u. to 0.005 a.u. has only minor effects on the essential spectral features. The larger value effectively smooths the simulated absorption signal.

Simulating the pump-probe signal required much larger trajectory ensembles

than our earlier study of the final product distributions [15], because only a small portion of the ensemble contributes to the absorption signal in a particular time window. For each cluster size studied, 250 trajectories were computed from starting configurations obtained by sampling a single 2.5 ns trajectory with an average temperature of 80 K. The dissociation and recombination times vary from a few picoseconds to over 75 ps in some cases where I_2^- is temporarily trapped in an excited electronic state. Since we are primarily interested in short time dynamics most of the simulations were terminated at 20 ps, although we did run one ensemble of 100 trajectories out to 100 ps in order to establish the asymptotic behavior. To compensate for the smaller size of this ensemble, the time width, σ_t , was increased to 300 fs.

5.2 Results and Discussion

5.2.1 $I_2^-(CO_2)_{16}$

In Fig. 5.2 we compare our simulated absorption recovery signal with the experiments of Papanikolas et al. [2, 30]. The simulation clearly reproduces the transient absorption feature at 2 ps. We have found the transient in two separate 250-trajectory simulations of $I_2^-(CO_2)_{16}$ photodissociated at 720 nm, in a simulation using a lower pump frequency (790 nm), and in simulations of I_2^- clustered with 10, 12, and 14 CO_2 molecules. The intensity of the 2 ps bump relative to the overall absorption recovery is lower in the simulation than in the experiment, but this is hard to interpret since the measured two-photon product signal depends on photofragment branching ratios as well as the transition moments for probe absorption; for now we make only qualitative comparisons.

While the short-time dynamics is well reproduced, Fig. 5.2(a) shows that at longer times the absorption recovery is significantly slower in the simulations than in the experiment. Margulis and Coker found a similar discrepancy in their simula-

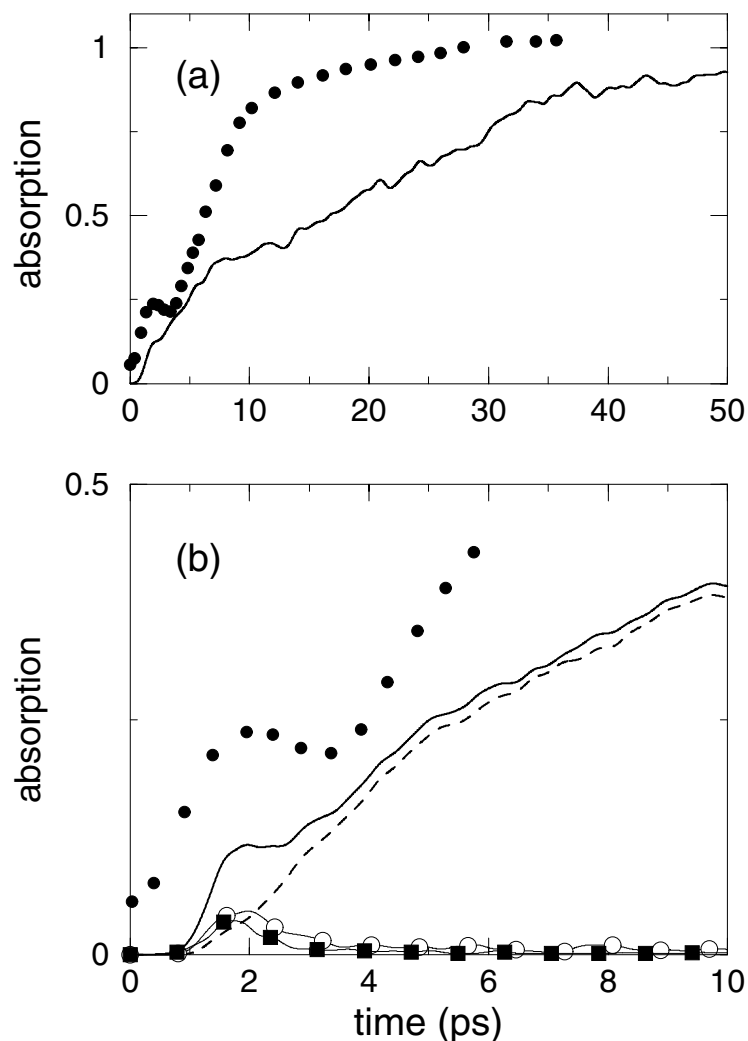


Figure 5.2: Absorption recovery of $I_2^- CO_{16}$ (a) Comparison of experimental (dots) and simulated (line) signals. Simulated signal is from 100-trajectory ensemble and reaches its asymptotic value between 60 and 80 ps. (b) Solid line is the total simulated signal from a 250-trajectory ensemble, dots are the experimental data. Dashed line is the contribution from the $X \rightarrow A'$ transition. The transient feature at 2 ps is due to $X \rightarrow a'$ and $X \rightarrow B$ transitions, shown respectively by the open circles and filled squares.

tion [18], and attributed it to trajectories that become trapped in the intermediate A state for long times before relaxing to the ground state. A -state trapping was also seen in our own previous study [16], in which we calculated the time-dependent state populations but not the absorption recovery. While the FPES experiments of Neumark and coworkers provide evidence that A -state recombination does indeed occur [12], the associated

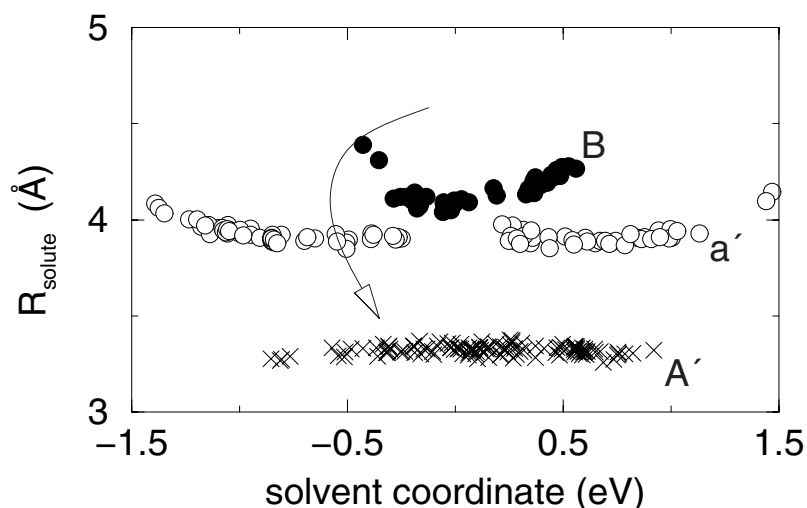


Figure 5.3: Location of strong, 720 nm absorption regions in the $(R, \Delta\Phi)$ plane. Transitions originate on the X state and end on the A' (x's), a' (open circles), and B (filled circles) states. Arrow represents simplified pathway for trajectories recombining on the X state.

spectral features disappear in a few ps, implying that both simulations underestimate the rate of $A \rightarrow X$ electronic quenching. Since the two simulation models are constructed in very different ways, we infer that the disagreement with experiment is due to some physical approximation common to both, such as the neglect of intramolecular CO_2 vibrations, rather than to incidental details of the potentials.

In Fig. 5.2(b) we decompose the total absorption according to the initial and final states involved in the transitions. While the overall rise is dominated by absorption from the ground state to the A' excited state (i.e. the same transition that initially dissociated the molecule), the 2 ps transient is entirely due to transitions from the ground state to the a' and B excited states, which correlate to spin-orbit excited iodine (I^*). Although the A state is populated, transitions originating on this state make a negligible contribution to the signal, because trajectories on the A state never find regions where such transitions would be resonant with the 720 nm probe, as will be discussed below.

To further elucidate the origin of the 2 ps peak, we map the trajectories using two coordinates: R , the solute bondlength, and $\Delta\Phi$, a collective solvent coordinate defined

as the change in energy when a unit charge is moved from one I atom to the other holding all nuclear coordinates fixed. The magnitude of $\Delta\Phi$ is small for symmetric solvent configurations around the solute, and large for asymmetric configurations in which one I atom is preferentially solvated. We monitor R and $\Delta\Phi$ along the simulation trajectories and record those points for which the contribution of the trajectory to the probe absorption exceeds a threshold value. The resulting plot, Fig. 5.3, displays the solute and solvent configurations that give rise to the various components of the probe absorption. The $X \rightarrow A'$ transitions occur primarily near the equilibrium bond distance, confirming the previously accepted conclusion that the overall absorption recovery is due to recombination followed by vibrational relaxation on the ground state [2, 4]. The transitions to the spin-orbit excited a' and B states occur at larger internuclear distances, as I_2^- recombines.

The markedly different shapes of the high intensity regions mapped out by the $X \rightarrow a'$ and $X \rightarrow B$ transitions reflect the strong dependence of the corresponding state energies on the solvent coordinate [7, 15, 16, 20]. Since the X and a' states both have ungerade symmetry in the isolated molecule, the $X \rightarrow a'$ transition is forbidden at $\Delta\Phi = 0$ but becomes allowed in highly asymmetric solvent environments. The $X \rightarrow B$ transition, in contrast, is strongest in symmetric environments. The X and a' states are stabilized by solvent asymmetry, so that at fixed R the energy gap between these states depends weakly on $\Delta\Phi$. In contrast, the B state is destabilized in an asymmetric cluster, so that the energy of this state increases with $\Delta\Phi$. Since the X and B state energies move in opposite directions as $\Delta\Phi$ increases away from zero, the energy gap between these states depends strongly on $\Delta\Phi$ at fixed R , so that it is necessary to vary both R and $\Delta\Phi$ in order to keep the gap constant. This leads to the highly curved profile mapped out by the $X \rightarrow B$ transition.

Prior to this study, the 2 ps feature had been attributed to absorption from the inner turning point on the A state to the a state. The semi-empirical potential curves

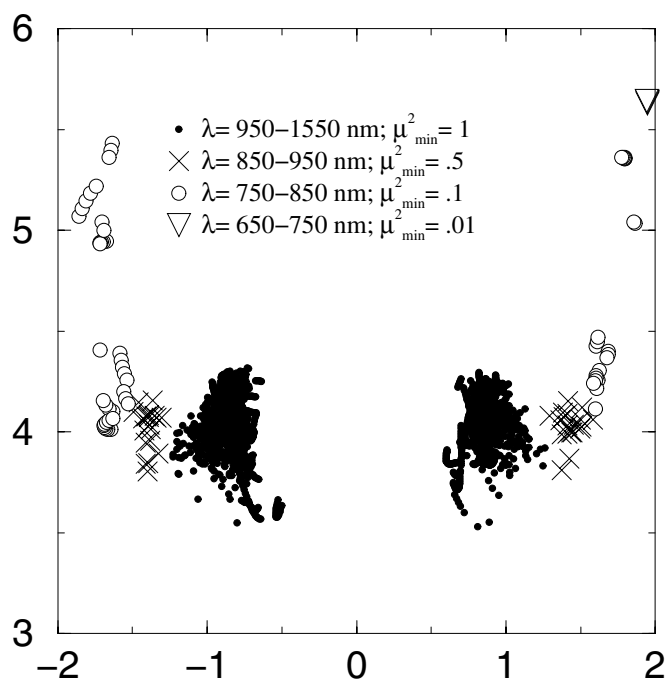


Figure 5.4: Map of $A \rightarrow a$ transitions centered at wavelengths from 700–1500 nm. Note that transition intensity is diminished at the smaller wavelengths.

available for I_2^- at that time [31] indicated that the transition would be resonant with 720 nm at a solute bondlength just slightly smaller than the equilibrium bondlength for the A state. However, more recent **ab initio** calculations from our group [21] and experiments by Neumark and co-workers [32] have produced more accurate I_2^- gas phase potentials. On the calculated surfaces shown in Fig. 5.1, the $A \rightarrow a$ energy gap is 1.72 eV at $R_{\text{solute}} \approx 2.9 \text{ \AA}$. This point is so far up the A state repulsive wall that it is higher in energy than the asymptote of the upper spin-orbit manifold. Furthermore, simulations of the photodissociation dynamics show that motion on the A state is diffusive rather than coherent and so we do not expect the A state population to give rise to a distinct peak in the probe absorption.

As noted repeatedly in this study, the gas phase curves, alone, cannot be used to rule out a mechanism, since the solvent configuration profoundly alters the I_2^- potentials. In this particular case, the effect of solvent asymmetry is dramatic because the A

and a states exhibit opposite charge flow character. In the vicinity of the A state well ($R_{\text{solute}} \approx 4 \text{ \AA}$), the energy gap between the A and a states varies from about 350 meV at zero solvent coordinate to 1.55 eV at $|\Delta\Phi| = 1.75 \text{ eV}$. This is illustrated in Fig. 5.4, which plots the points at which trajectories on the A state pass through regions which are above a threshold absorption strength to the a state, analogous to Fig. 5.3. A range of probe wavelengths, from 700 nm (1.77 eV) to 1500 nm (0.83 eV), are shown. The only transitions comparable in strength to the $X \rightarrow A'$ (pump) transition are at wavelengths greater than 1000 nm. For shorter wavelengths, a lower threshold value of μ^2 is used to uncover where these resonances occur. Transitions with $\lambda = 700 \pm 50 \text{ nm}$ are at least two orders of magnitude lower in intensity than the $X \rightarrow A'$ transitions and occur only at the most extreme solvent coordinates accessed in the simulations ($|\Delta\Phi| \geq 2 \text{ eV}$). In principle, there is a horseshoe shaped region of resonance with 720 nm, however, these areas of the potential curves are not energetically accessible.

5.2.2 Cluster-Size Dependence

Figure 5.5(a) shows the total simulated 720 nm absorption recovery signals for $I_2^-(\text{CO}_2)_{n=10,12,14,16}$. As in the experiment, intermediate cluster sizes show multiple relaxation timescales, and for $n \geq 13$ a shoulder in the absorption signal develops into a transient peak at about 2 ps. Figure 5.5(b) shows the same signal separated into contributions from the $X \rightarrow A'$ and $X \rightarrow (a',B)$ transitions. For $n = 14$ and 16, the transient peak, due to $X \rightarrow (a',B)$ transitions, is mostly localized at 2 ps, where the contributions from the $X \rightarrow A'$ transition are very small. For the smaller cluster sizes, the transient peak is spread out over a longer time period and overlaps with contributions from the $X \rightarrow A'$ transition. The net result is a less distinct transient feature, however the integrated intensity of the transient peak from $n = 10$ is more than twice that from $n = 16$, see Table 5.1.

A factor affecting the intensity of the transient peak is the amount of time the

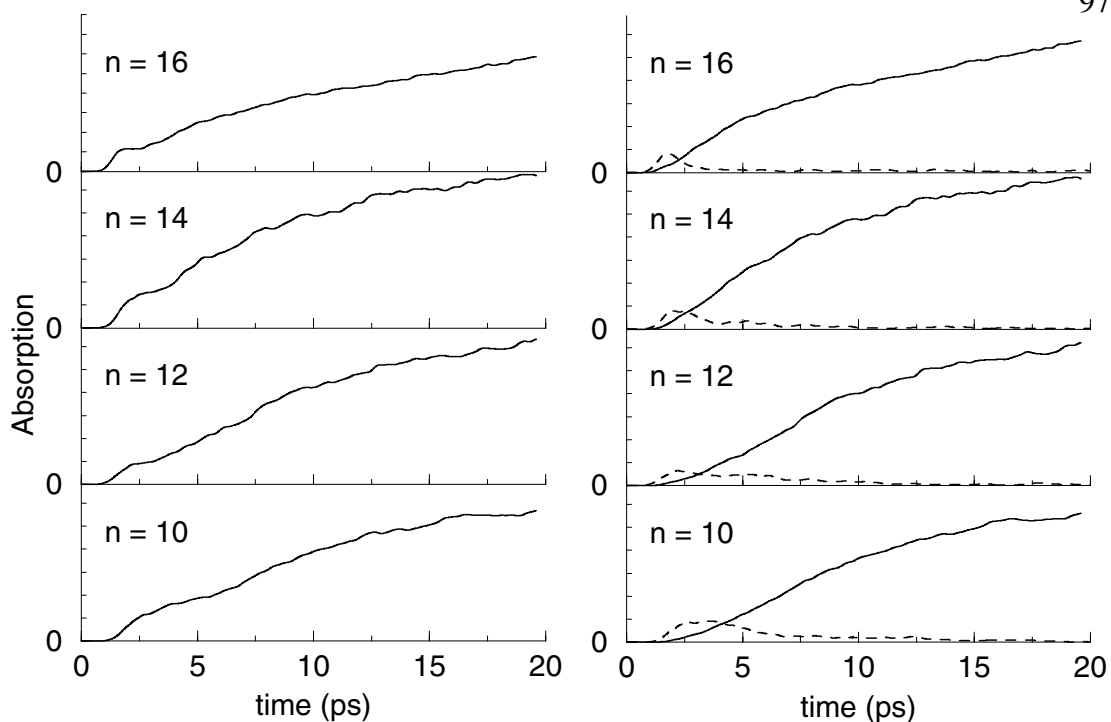


Figure 5.5: Simulated absorption recovery signals for $\text{I}_2^-(\text{CO}_2)_n$ clusters. (a) Total signal. (b) Decomposed by final spin-orbit state, solid line: A' , dashed line: a' and B .

clusters spend in the absorption window. Since the transitions to the spin-orbit excited states take place only at solute bondlengths greater than 3.75\AA , the rate of vibrational relaxation on the ground electronic state, which is dependent on the cluster size, will in part determine the prominence of the transient peak. The average solute bondlength versus time for cluster sizes $n = 10$ and 16 is shown in Fig. 5.6. Since we wish to focus on the vibrational relaxation process, we subtract off the time required for electronic relaxation by resetting the time origin for each trajectory such that $t_0 = t_{\text{recombination}}$. At $t = 0$ on this plot, each trajectory has just passed through the absorption window. Trajectories from the $n = 10$ ensemble return to this region at least two additional times, while trajectories from the $n = 16$ ensemble relax below the threshold bondlength sooner.

The strength of the transition dipole also depends on the solvent coordinate as

Table 5.1: Integrated intensity of transient peak vs. n

n	Intensity
10	2.1
12	1.7
14	1.3
16	1

shown in Fig. 5.3. We find that the larger the cluster, the more rapidly the solvent asymmetry decreases following recombination. For trajectories in the $n = 16$ ensemble, the solvent coordinate is nearly zero after the first compression of the I_2^- bond. At this small value of $\Delta\Phi$, only the $X \rightarrow B$ transition has appreciable strength and the threshold value for the solute bondlength is greater than 4\AA . Therefore, as the cluster size increases from $n = 10$ to 16, I_2^- spends less time in the regions that contribute to the transient absorption peak.

In summary, the integrated intensity of the transient feature in the simulated pump-probe spectrum is actually greater in $I_2^-(CO_2)_{10}$ than in $I_2^-(CO_2)_{16}$, but the transient appears more **distinct** in the larger clusters, in agreement with the experiments. The prominence of the transient peak in the larger clusters is due to a component of the ensemble which passes through the absorption window within a narrow time window prior to the accumulation of population in the bottom of the I_2^- vibrational well.

5.2.3 $I_2^-Ar_{20}$

If slightly slower vibrational relaxation increases the intensity of the transient absorption feature, as observed for $I_2^-(CO_2)_{10}$ relative to $I_2^-(CO_2)_{16}$, shouldn't the effect be even more prominent in a system with a vibrational relaxation timescale that is orders of magnitude longer than the electronic relaxation timescale? $I_2^-Ar_{20}$ clusters are an ideal system for testing this suggestion. Experiments [6, 11, 12] and simulations [17] have demonstrated that while relaxation to and recombination on the ground electronic

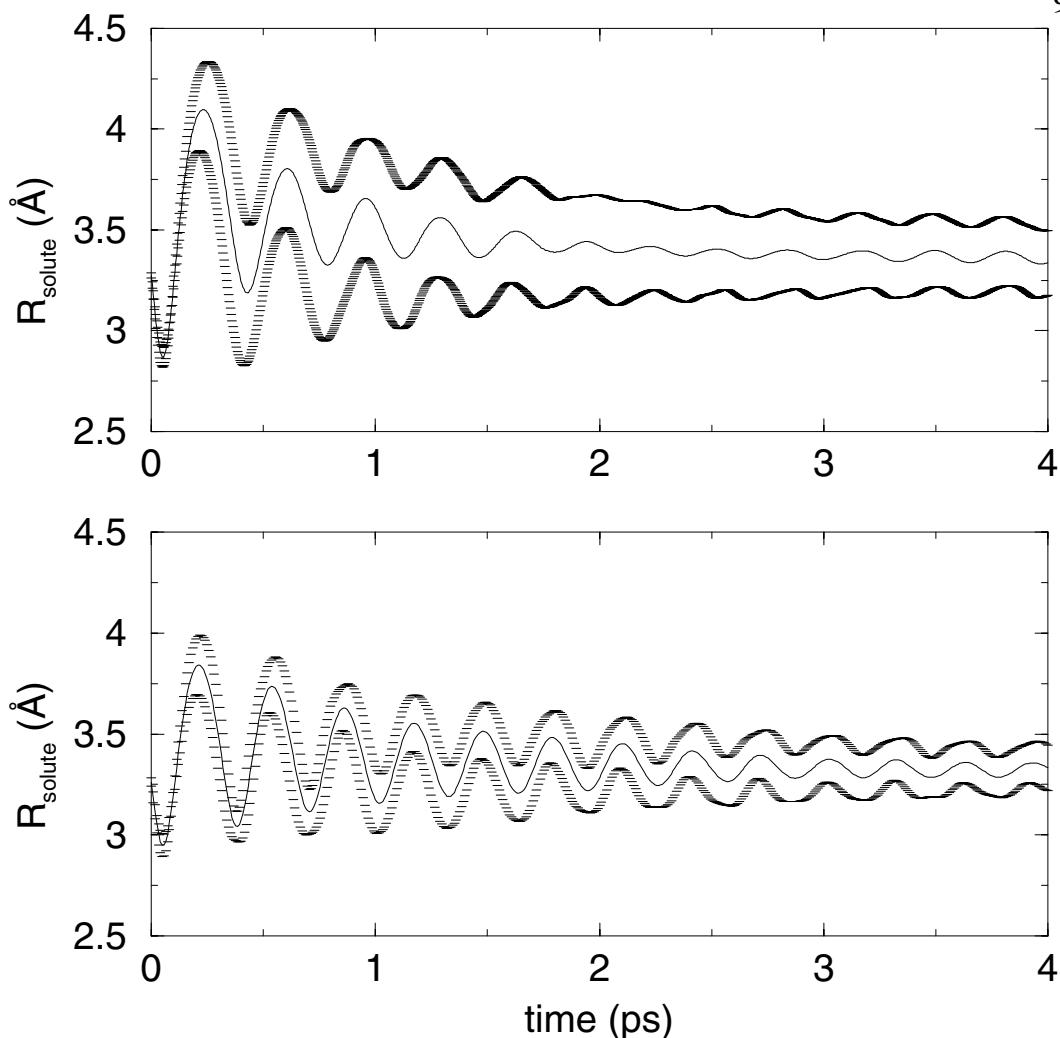


Figure 5.6: Ensemble average of the solute bondlength after recombination for $I_2^-(CO_2)_n$ (a) $n = 10$ and (b) $n = 16$.

state occurs within 5-10 ps after excitation, complete vibrational relaxation requires upwards of 200 ps.

Figure 5.7 shows the calculated absorption recovery for $I_2^-Ar_{20}$ with the pump and probe wavelength of 790 nm. The total signal (heavy solid line) is characterized by an intense peak at about 7 ps and a long time tail which levels off beyond 200 ps. Virtually all of the 790 nm spectrum arises from transitions originating on the X state of I_2^- . The signal corresponding to the $X \rightarrow A'$ (pump) transition, shown by the (dashed) line, rises monotonically from 3–200 ps. The peak at early time, including the

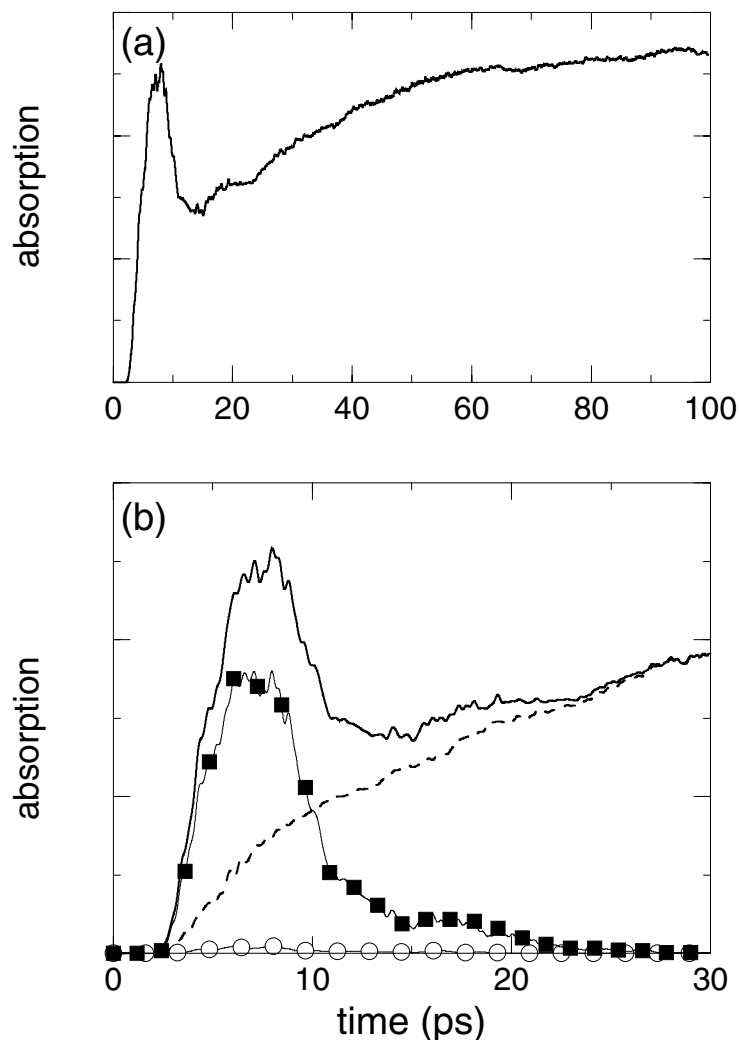


Figure 5.7: Absorption recovery of $\text{I}_2^- \text{Ar}_{20}$ (a) Total simulated signal. (b) Solid line is the total simulated signal from a 250-trajectory ensemble, dots are the experimental data. Dashed line is the contribution from the $X \rightarrow A'$ transition. The transient feature at 2 ps is due to $X \rightarrow a'$ and $X \rightarrow B$ transitions, shown respectively by the open circles and filled squares.

shoulder which extends to 25 ps, is due to the $X \rightarrow B$ transition. There is a very small contribution from the $X \rightarrow a'$ transition from 5–10 ps.

Figure 5.8 plots the regions of greatest transition strength at 790 nm visited by the trajectories as a function of the solute bondlength and the solvent coordinate. The $X \rightarrow B$ transition is resonant with 790 nm at $R_{\text{solute}} = 4.2\text{--}4.3 \text{ \AA}$. As described

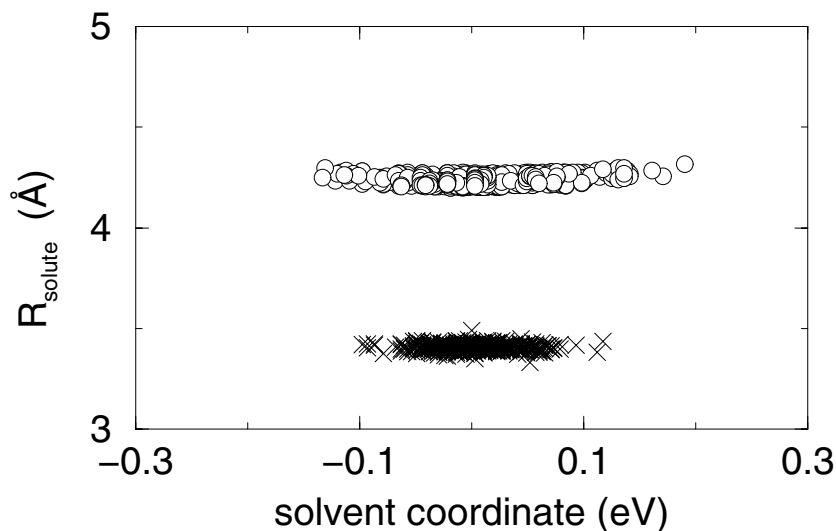


Figure 5.8: Location of strong, 790 nm absorption regions in the $(R, \Delta\Phi)$ plane. Transitions originate on the X state and end on the A' (x's) and B (filled circles) states. Arrow represents simplified pathway for trajectories recombining on the X state.

in Section 5.2.1, the intensity of this transition is strongest as $|\Delta\Phi|$ nears zero. The solvent coordinate is restricted to much smaller magnitudes in argon relative to CO_2 and therefore trajectories do not pass through the Franck-Condon regions for strong $X \rightarrow a'$ transitions located at large solvent coordinates for $R_{\text{solute}} \leq 4 \text{ \AA}$.

The experimental absorption recovery signal measured by Vorsa et al. is a smoothly rising curve, similar to the contribution from the $X \rightarrow A'$ transition of our simulated signal. The complete lack of evidence for transient absorption in the experimental signal appears to be in direct conflict with the simulated spectrum, but before drawing this conclusion, we must reconsider what was actually observed in the experiments. The pump-probe signal is not a direct absorption measurement, but rather an action spectrum. That is, a secondary effect of absorption is measured and used to infer the absorption signal. In the present case, it is the mass distribution of photodissociation and recombination products that is observed directly. To generate the absorption recovery signal at a given time delay, the mass spectrum is measured and all of the products

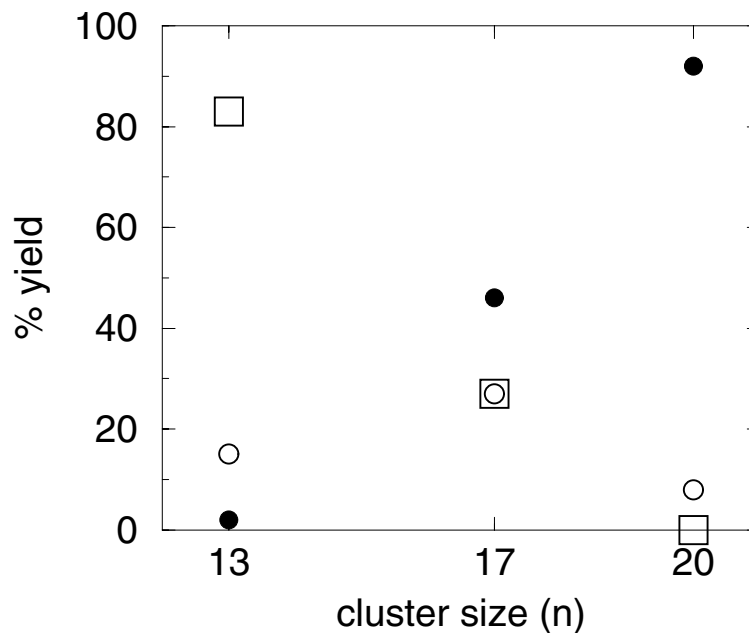


Figure 5.9: UV photodissociation products. Squares: dissociation on the B state. Open circles: dissociation on the a' state. Filled circles: metastable recombination on the a' state.

corresponding to two-photon absorption are added together. The signal is normalized to the number of two-photon products detected at an effectively infinite time delay. However, this method requires **a priori** knowledge of what constitutes a two-photon product and that the one- and two-photon product channels are mass-separable. Our simulations of the absorption recovery indicate that the transient absorption is due to the $X \rightarrow (a', B)$ transition. We must ask, “What are the final products if the second pulse promotes I_2^- to the spin-orbit excited states?”

To address this question, we have simulated the photodissociation of $I_2^- Ar_n$ clusters at 395 nm. This ultraviolet pulse excites I_2^- to the B electronic state. Three product channels are observed: dissociation on the B state, dissociation on the a' state, and metastable recombination on the a' state. The branching ratios between these products for cluster sizes $n = 13, 17$, and 20 are shown in Fig. 5.9. We do not observe any relaxation to the lower spin-orbit states of I_2^- . This is consistent with the mechanism

for spin-orbit relaxation of $I_2^-(CO_2)_n$ clusters discussed in Chapter 4.

The key step in the relaxation process involves bringing states of the upper and lower spin-orbit manifolds together in energy. This is possible because of the large differences in the solvent potential at each iodine atom which occur in asymmetric $I_2^-(CO_2)_n$ clusters. In contrast, the solute-solvent interactions are much weaker in $I_2^-Ar_n$ clusters, and the maximum magnitude of the solvent coordinate which can be attained with 20 argon atoms is only about a third of spin-orbit splitting energy of iodine. This explains why no products on the lower spin-orbit states are observed.

Consider now the excitation of I_2^- to the B state by the probe photon. The absorption originates on the X electronic state at a solute bondlength of roughly 4.4 Å. At this bondlength, the B state has nearly reached its dissociative limit. In the absence of a mechanism for spin-orbit relaxation, the photon energy is almost entirely converted into electronic energy of spin-orbit excited iodine and there is virtually zero kinetic energy released. This means that no additional solvent molecules are evaporated from the cluster and the photoproducts are identical to the products following absorption of only the pump pulse. Therefore, these products would be excluded from the experimental two-photon signal and no transient absorption feature would be detected.

The experimental signal should be compared to the overall rise of the simulated spectrum, which is due to the $X \rightarrow A'$ contribution. This is shown in Fig. 5.10. Although there is some ambiguity as to whether either signal has truly reached its asymptotic behavior, the simulated signal shows a faster initial recovery. The time scales for electronic and vibrational relaxation from our simulations agree well with those determined from FPES experiments [11, 17, 33] and so it is not clear what causes the discrepancy between these two pump-probe signals. One source of error may be the bondlength dependence of the transition dipole strengths as determined by our **ab initio** calculations.

Finally, we note that the fact that the transient peak involves excitation to the spin-

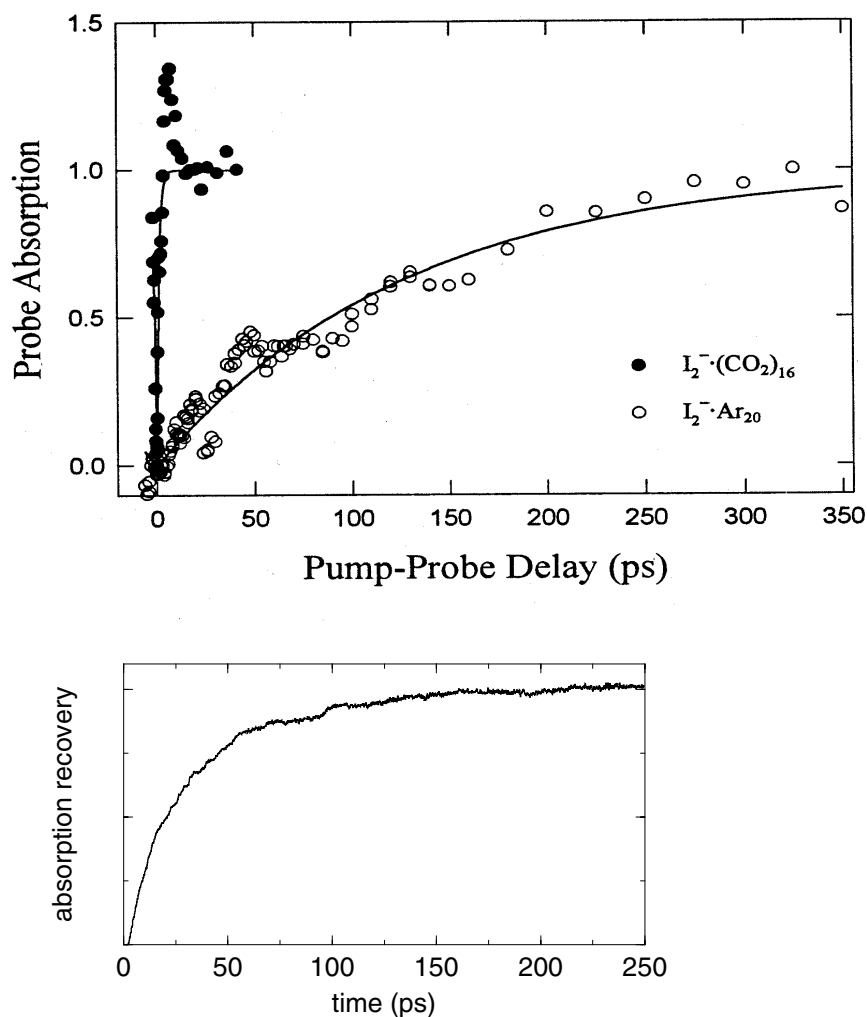


Figure 5.10: Absorption recovery of $I_2^- \cdot Ar_{20}$. Top panel shows experimental results from Ref. 6. Bottom panel shows longtime behavior of simulated spectrum.

orbit excited states affects the interpretation of the absorption recovery of $I_2^-(CO_2)_n$ clusters as well. While there is a mechanism for spin-orbit relaxation in these systems, the probability for return to the lower manifold varies with cluster size and is less than one at $n = 16$. Thus it is possible that some of the two-photon products are missing from the experimental signal in this system as well. Additional molecular dynamics simulations may be able to determine whether these products are separable from the one-photon products. This should be investigated before a quantitative comparison between the experimental and simulated absorption spectra is made.

5.3 Conclusions

Figures 5.2 and 5.3 lead to a physical picture for the photodissociation/recombination process in $\text{I}_2^-(\text{CO}_2)_n$ clusters that ties together the insights derived from earlier studies. After dissociation, some members of the ensemble temporarily recombine on the A state, but others hop directly to the ground state in less than 2 ps [16, 18]. As I and I^- recombine on the X state, they pass through the strong $X \rightarrow (a', B)$ absorption region at $R=4-5$ Å. This initial coherent passage gives rise to the 2 ps transient peak. Since recombined I_2^- loses energy very rapidly to the solvent, particularly near the top of the ground state well [34, 35], it never returns to the large- R absorption region, so the transient is not repeated. Instead, the solute relaxes vibrationally, giving rise to the main $X \rightarrow A'$ absorption recovery. This rapid vibrational relaxation is accompanied by a rapid loss of coherence in the ensemble, as seen in Fig. 5.6. At longer times the recovery signal is dominated by the slow build-up of population on the X state as the A state is electronically quenched, rather than by the very fast X -state vibrational relaxation. Since the simulations underestimate the electronic quenching rate, they overestimate the time scale for overall absorption recovery.

In summary, our simulations provide strong evidence that the 2 ps peak in the absorption recovery signal is due to transitions from the ground state to the spin-orbit excited states of I_2^- , not to transitions originating on the intermediate A state. The transient absorption occurs as the photofragments first begin to recombine, rather than at the inner turning point, and is strongly influenced by the solvent environment. The transient is not seen experimentally in I_2^-Ar_n clusters because there is no efficient mechanism for quenching the spin-orbit excitation energy, and therefore the final products from these transitions are not included in the two-photon mass signal. This reassignment is consistent with all of the experimental evidence, and reinforces the physical picture of the recombination dynamics that has emerged from earlier simulations.

References for Chapter 5

- [1] J. Papanikolas, V. Vorsa, M. Nadal, P. Campagnola, J. Gord, and W. C. Lineberger, *J. Chem. Phys.* **97**, 7002 (1992).
- [2] J. Papanikolas, V. Vorsa, M. Nadal, P. Campagnola, H. Buchenau, and W. C. Lineberger, *J. Chem. Phys.* **99**, 8733 (1993).
- [3] J. M. Papanikolas, *I₂⁻ Photodissociation and Cage Recombination Dynamics in Size-Selected I₂⁻(CO₂)_n Clusters*, PhD thesis, University of Colorado, 1994.
- [4] D. A. V. Kliner, J. C. Alfano, and P. F. Barbara, *J. Chem. Phys.* **98**, 5375 (1993).
- [5] P. K. Walhout, J. C. Alfano, K. A. M. Thakur, and P. F. Barbara, *J. Phys. Chem.* **99**, 7568 (1995).
- [6] V. Vorsa, S. Nandi, P. J. Campagnola, M. Larsson, and W. C. Lineberger, *J. Chem. Phys.* **106**, 1402 (1997).
- [7] S. Nandi, A. Sanov, N. Delaney, J. Faeder, R. Parson, and W. C. Lineberger, *J. Phys. Chem. A* **102**, 8827 (1998).
- [8] A. E. Johnson, N. E. Levinger, and P. F. Barbara, *J. Phys. Chem.* **96**, 7841 (1992).
- [9] G. Ashkenazi, U. Banin, A. Bartana, R. Kosloff, and S. Ruhman, *Adv. Chem. Phys.* **100**, 317 (1997).
- [10] A. Sanov, S. Nandi, and W. C. Lineberger, *J. Chem. Phys.* **108**, 5155 (1998).
- [11] B. J. Greenblatt, M. T. Zanni, and D. M. Neumark, *Science* **276**, 1675 (1997).
- [12] B. J. Greenblatt, M. T. Zanni, and D. M. Neumark, *Faraday Discuss.* **108**, 101 (1997).
- [13] V. S. Batista and D. F. Coker, *J. Chem. Phys.* **106**, 7102 (1997).
- [14] J. Faeder, N. Delaney, P. Maslen, and R. Parson, *Chem. Phys. Lett.* **270**, 196 (1997).

- [15] N. Delaney, J. Faeder, P. E. Maslen, and R. Parson, *J. Phys. Chem. A* **101**, 8147 (1997).
- [16] J. Faeder, N. Delaney, P. Maslen, and R. Parson, *Chem. Phys.* **239**, 525 (1998).
- [17] J. Faeder and R. Parson, *J. Chem. Phys.* **108**, 3909 (1998).
- [18] C. Margulis and D. F. Coker, *J. Chem. Phys.* **110**, 5677 (1999).
- [19] A. Sanov, T. Sanford, S. Nandi, and W. C. Lineberger, *J. Chem. Phys.* **111**, 663 (1999).
- [20] N. Delaney, J. Faeder, and R. Parson, *J. Chem. Phys.* **111**, 651 (1999).
- [21] P. E. Maslen, J. Faeder, and R. Parson, *Chem. Phys. Lett.* **263**, 63 (1996).
- [22] A. J. Stone, *The Theory of Intermolecular Forces*, Oxford, New York, 1996.
- [23] Y. Zhao, C. C. Arnold, and D. M. Neumark, *J. Chem. Soc. Faraday Trans.* **89**, 1449 (1993).
- [24] C. S. Murthy, S. F. O'Shea, and I. R. McDonald, *Mol. Phys.* **50**, 531 (1983).
- [25] L. Verlet, *Phys. Rev.* **159**, 98 (1967).
- [26] M. P. Allen and D. J. Tildesley, *Computer Simulation of Liquids*, Clarendon Press, Oxford, 1987.
- [27] J. C. Tully, *J. Chem. Phys.* **93**, 1061 (1990).
- [28] S. Hammes-Schiffer and J. C. Tully, *J. Chem. Phys.* **101**, 4657 (1994).
- [29] V. S. Batista and D. F. Coker, *J. Chem. Phys.* **106**, 6923 (1997).
- [30] We compare to the “magic angle” absorption recovery, Fig. 9a of Ref. 2, in which the effects of cluster rotation have been removed by averaging the two absorption signals measured with the probe parallel and perpendicular to the pump. This is the appropriate signal with which to compare our simulation, because our calculated absorption intensities do not take into account the orientation of the transition dipole in the laboratory frame.
- [31] E. C. M. Chen and W. E. Wentworth, *J. Phys. Chem.* **89**, 4099 (1985).
- [32] M. T. Zanni, V. S. Batista, B. J. Greenblatt, W. Miller, and D. M. Neumark, *JCP* **110**, 3748 (1999).
- [33] B. J. Greenblatt, *Femtosecond Photoelectron Spectroscopy: A New Tool for the Study of Anion Dynamics*, PhD thesis, University of California, 1999.
- [34] I. Benjamin, P. F. Barbara, B. J. Gertner, and J. T. Hynes, *J. Phys. Chem.* **99**, 7557 (1995).

- [35] J. M. Papanikolas, P. E. Maslen, and R. Parson, *J. Chem. Phys.* **102**, 2452 (1995).